AIP Journal of Applied Physics

Shielding of optical pulses on hydrodynamical time scales in laser-induced breakdown of saline water

D. Conti-Sampol, F. Marino, G. Roati, A. Orfila, J. Javaloyes, O. Piro, and S. Balle

Citation: Journal of Applied Physics **116**, 033102 (2014); doi: 10.1063/1.4890313
View online: http://dx.doi.org/10.1063/1.4890313
View Table of Contents: http://scitation.aip.org/content/aip/journal/jap/116/3?ver=pdfcov
Published by the AIP Publishing

Shielding of optical pulses on hydrodynamical time scales in laser-induced breakdown of saline water

D. Conti-Sampol,[1] F. Marino,[2] G. Roati,[3,4] A. Orfila,[1] J. Javaloyes,[5] O. Piro,[5] and S. Balle[1,5]
[1]*Institut Mediterrani d'Estudis Avançats (CSIC-UIB), C/ Miquel Marqués, 21, 07190 Esporles, Spain*
[2]*CNR-Istituto Nazionale di Ottica, largo E. Fermi 6, I-50125 Firenze, Italy*
[3]*CNR-Istituto Nazionale di Ottica, via Nello Carrara 1, I-50019 Sesto Fiorentino, Italy*
[4]*LENS and Dipartimento di Fisica e Astronomia, Università di Firenze, via Sansone 1, I-50019 Sesto Fiorentino, Italy*
[5]*Dept. de Física, Univ. Illes Balears, Ctra. De Valldemossa km. 7'5, 07122 Palma de Mallorca, Spain*

(Received 22 May 2014; accepted 3 July 2014; published online 17 July 2014)

Pulse shielding in Laser-Induced Breakdown of saline water on hydrodynamic time scales is experimentally characterized. Pairs of pulses from a Nd:YAG laser are focused into saline water with a controlled time delay between them. The Laser-Induced Breakdown produced by the first pulse creates a cavitation bubble that later collapses generating a plume of bubbles that evolves on hydrodynamic time scales. When the second pulse arrives, the light is scattered by this plume with a consequent reduction in the intensity at the focal spot resulting in a lower breakdown efficiency of this pulse. By means of acoustic measurements, we determine the breakdown energy threshold for the first pulse and characterize the shielding of the second pulse as a function of the salinity of the solution, the energy of the pulse, and the inter-pulse interval. A model for the blocking process that takes into account both linear and nonlinear absorption along the path is developed which satisfactorily explains the observations. © *2014 AIP Publishing LLC*.
[http://dx.doi.org/10.1063/1.4890313]

I. INTRODUCTION

Tightly focused laser pulses can deposit large energy densities in reduced volumes during a short time interval. This capability may be used to induce structural, morphological, or physico-chemical transformations in specific locations of materials.[1] In particular, massive material removal from a target can be achieved under the action of laser pulses of a sufficiently high intensity. This procedure, named *laser ablation*, has a wide range of applications, such as laser surgery,[2] mass-spectrometry,[3] as well as deposition and microstructuring of thin films and coatings,[1,4] instances that have been under continuous active research during the past two decades. More recently, laser ablation has been also applied to problems in the domain of nanotechnology for machining of structures below the optical diffraction limit,[5] synthesizing fullerenes, carbon nanotubes[6] or Si nanowires,[7] and generating nanoparticles or nanocrystalline structures.[1,4,8,9]

In addition to their interest for applications, these laser pulses allow also to explore the nonlinear mechanisms of interaction between light and matter. In transparent media subject to high enough irradiance, Laser-Induced Breakdown (LIB) may occur by multiphoton ionization followed by avalanche ionization. These processes lead to the formation of a hot plasma that rapidly expands generating a pressure shock-wave (see Ref. 10 for a recent review). If the medium is a liquid, a cavitation bubble is formed by vaporization in the breakdown region. Initially at high pressure and temperature, this cavity first expands itself and later eventually collapses, dissipating energy in the form of acoustic waves. This phenomenon has been extensively studied especially in water[11] because of its relevance in biological and medical applications, but also because it serves as a model to study hydrodynamical processes triggered by a sudden and localized deposition of energy in a fluid.

From the collapse of the cavitation bubble, a cloud of smaller bubbles emerges and moves under the combined action of buoyancy forces and the flow generated in the fluid by the acoustic wave. If a second laser pulse is sent through the fluid before this cloud settles, the bubbles would scatter-off part of the light with a consequent reduction of the irradiance at the focus.[12] This kind of attenuation or shielding of the successive pulse has a duration much longer than that of the pulse and the lifetime of the subsequent luminous plasma. Nahen and Vogel[13] have shown that for Er:YAG laser pulses of 200 μs on water, the ejected plume induces rather large attenuation (of a strength that depends on the pulse energy) not showing any signs of recovery up to 350 μs after the delivery of the first pulse. Similarly, Murray and Dickinson[14] have shown that the attenuation due to the ablation plume ejected from a dentine sample lasts for about 7 ms.

The above mentioned shielding of the successive pulse with a lifetime on hydrodynamic time scales is generic in the interaction of laser radiation with fluid environments of either liquid or gaseous nature. The time scales involved depend on the fluid environment but in every case shielding has an obvious impact on applications. It implies, for example, a reduction of the efficiency (ablated mass per pulse) in the production of nanoparticles,[15] which obliges to devise strategies to bypass the phenomenon. This need has stimulated intense theoretical work devoted to modeling the evolution of the plume and its impact on the laser pulses. One line of research has focused on the hydrodynamics of the plume as described by Navier-Stokes equations,[16–19] while others use phenomenological approaches for describing the state of the plume.[20,21]

In all these instances, however, attenuation of the light pulses is assessed by means of the Lambert-Beer's law that yields an exponential decay of the intensity of the beam as it propagates. However, this law is only valid for linear absorption and not when nonlinear phenomena like multi-photon absorption have to be considered. In this case, the distribution of the light power along the propagation axis differs significantly from a simple exponential decay and more elaborated tools of analysis are required in order to determine the beam profile under propagation. Sophisticated numerical approaches have been developed in order to simulate the beam profile (see e.g., Ref. 22 for a review), although they all require intensive computation. On the other hand, some approximate methods to solve the equations describing the evolution of the beam profile have also been developed. One successful approximation valid in many circumstances is given by a variational technique known as "collective variable approach" (CVA) that was originally introduced by Anderson[23] for the study of the nonlinear Schrodinger equation and later extended to non conservative systems.[24–26] In the CVA, a sensible trial function is chosen to describe the field as it propagates,[24–26] with a number of properties (e.g., the intensity, phase and beam waist) being allowed to vary with propagation distance. These properties are treated as Rayleigh-Ritz optimization functions, and they are determined by minimisation of a reduced Lagrangian. This has allowed to obtain quite accurate results for the beam profile in different cases of nonlinear propagation, although it is clear that the closer the trial function is to the actual solution, the more accurate the results.

In this paper, we study, by means of acoustic measurements,[27] the hydrodynamic-time-scale dynamics of the pulse shielding by cavitation bubble clouds produced during Laser-Induced Breakdown of saline water. The advantage of the acoustic characterization of this phenomenon is that sound can be processed in real-time by the acquisition system in contrast with the long post-processing required for the analysis of optical images. In Sec. II, we characterize experimentally the pulse shielding for pairs of pulses delivered by a Nd:YAG laser focused into saline water at controlled inter-pulse time intervals. We determine the energy threshold for cavitation by an individual pulse and then characterize the shielding of the second of a pair of pulses as a function of salinity, pulse energy, and pulse-to-pulse delay. In Sec. III, we develop a model for the shielding process that comprises three different modules: (i) an optical module based on the CVA that describes the propagation of a Gaussian beam in a medium with both linear loss and multi-photon absorption; (ii) a bubble-generator module that describes the production of bubbles in the regions of high optical field intensities; and (iii) a hydrodynamic module that describes the movement of the bubbles driven by the fluid flow induced by the cavitation dynamics. The model allows us to explain satisfactorily the observed dependencies. Finally, we discuss our conclusions in Sec. IV.

II. EXPERIMENTAL SETUP AND MEASUREMENTS

A. Experimental setup

Our experimental setup is schematically shown in Fig. 1. A spectro-photometer quartz cuvette of internal dimensions

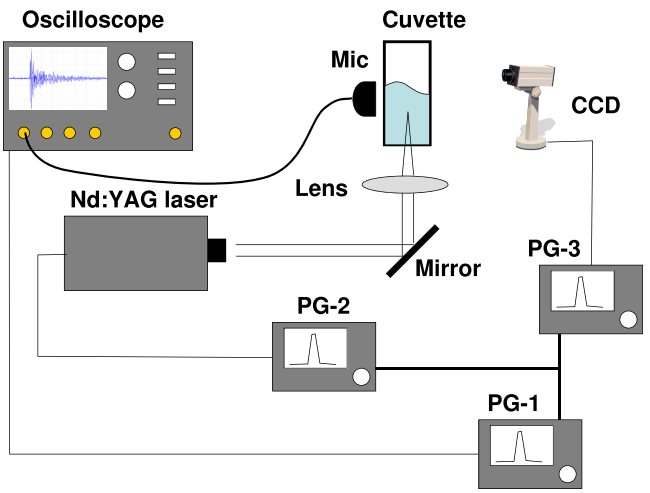

FIG. 1. Experimental setup (see text for a complete description).

10 mm × 10 mm × 50 mm, made of optical quality bottom and side walls is filled with a controlled dissolution of pure NaCl in distilled (milliQ) water. Pulses delivered by a Q-switched Nd:YAG laser (Quantel Ultra, $\lambda = 1064$ nm, 3 mm beam diameter with capabilities of up to up to 50 mJ per pulse and up to 100 pulses per second with external triggering) are focused through the bottom of the cuvette into the saline dissolution by means a plane-convex lens of focal length 50 mm. The duration of the laser pulses is 8 ns duration (full-width at half-maximum) and their energy can be adjusted into 2.5 mJ intervals. The system is monitored optically with a CCD camera connected to a computer, and acoustically with a microphone iBeat (20 Hz–20 kHz flat response, 32 Ω impedance) glued to the quartz cuvette and connected to a digital oscilloscope (LeCroy WaveTek 960, 2 GHz analog bandwidth). The quartz cuvette is illuminated by an array of red LEDs through a light diffuser to homogenize the intensity in order to produce and shadowgraph images of the fluid motion that are recorded by the CCD camera. Two different CCD cameras have been used: a low speed camera (Merlin) capable of shooting and capturing up to 15 frames per second (fps) with external triggering, and a high-speed camera (FasTech Troubleshooter HR) able to capture up to 2000 fps with a resolution of 640 × 480, and up to 16 000 fps at a reduced resolution of 32 × 1024.

A master generator PG-1 (HP 33210 A) is used to control the measurements and synchronize the instruments. On the rising edge of the signal, the digital scope is triggered to start acquisition. Simultaneously, two other arbitrary waveform generators PG-2 and PG-3 are triggered. The generator PG-3 provides the series of pulses that control acquisition of the images by the CCD camera. PG-2, in turn, generates the control signal for the Nd:YAG laser that may consist of either a single pulse during the determination of the ablation threshold or two pulses separated by a controlled time lapse for the investigation of the characteristics of pulse shielding. In both cases, we typically acquire 50 to 100 events with periods in the range from 5 to 10 s which are long enough to let the solution resettle into a quiescent state and the bubbles to disappear.

B. Breakdown threshold

In the first set of experiments, we deliver single laser pulses of fixed pulse energy into the saline solution and measure the intensity of the generated optical and acoustical response signals.

At low pulse energies, the fluid is slightly perturbed into some relatively slow state of motion after the application of the laser pulses without producing any detectable optical or acoustic emission. On the contrary, when the energy of the pulse is high enough, LIB takes place leading to the vaporization of the fluid through the formation of a plasma in the solution. The occurrence of this phenomenon can be recognized by the visualization of a blueish spark and an accompanying audible detonation. Fig. 2 shows the state of the solution at different times after the application of the laser pulse acquired with the fast CCD camera. When the plasma decays, a cloud of bubbles is formed within the solution. This cloud moves rapidly downwards at speeds of the order of 1 m/s. As the cloud of bubbles evolves, it breaks into several parts that start to fan out in the horizontal plane and, simultaneously, a liquid jet is formed at the interface between the liquid and the air. After a few milliseconds, the downwards motion of the cloud slows down at the vicinity of the cuvette's bottom and a concomitant horizontal dispersion of the bubbles takes place. Eventually, the bubbles begin to slowly ascend driven by buoyancy, until they finally vanish on time scales of the order of one second. This whole dynamics is accompanied by the emission of an audible acoustic wave that, upon conversion at the microphone, can be recorded by the oscilloscope as it is shown in Fig. 3(b).

The fast CCD camera is not always able to record the plasma emission during the earliest stages of the process (see, for instance, Fig. 2) because its shutter has a fixed 50% duty-cicle, and the jitter in the timing of the Q-switch of the laser sometimes makes the laser pulse occur when the shutter is closed. For the optical characterization of the process, we therefore use the slow CCD camera which, in turn, permits also the independent control of the shutter time and the CCD gain, although at the price of lower speed recording. We fix the exposure time to 1 ms—which guarantees the capture of the spark as it is shown in Fig. 3(a)—and we reduce the camera gain in order to avoid saturation in the images. The optical intensity is then computed by integrating the total intensity of each image. At the same time, the energy of the acoustic pulses is measured directly in the oscilloscope by means of few of its built-in signal processing functions. Specifically, for each laser pulse, we define a time window that covers the sound pulse recorded from the microphone and determine the acoustic power contained in this window by Fourier transforming the signal after filtering it with a running average over 10 samples and excluding frequencies above 17.5 kHz in order to reduce high-frequency noise. Background signals recorded with the laser shutter closed (i.e., in absence of laser pulses) are subtracted in both measurements. In all cases, 50–100 repetitions of the experiment are performed before the pulse energy is readjusted.

In Figs. 3(c) and 3(d), we show the dependence on the laser pulse energy of the intensities of the optical and acoustic signals emitted by the perturbed aqueous solution. For the sake of comparison, the intensities recorded with each instrument have been normalized to their maximum values. The acoustic measurements provide better linearity than the optical ones because of the higher noise floor in the CCD camera that is specially evident at low intensities. Although the CCD camera has a higher nonlinearity and background noise than the microphone, both indicators clearly reveal the existence of an energy threshold between 25 mJ and 30 mJ and exhibit

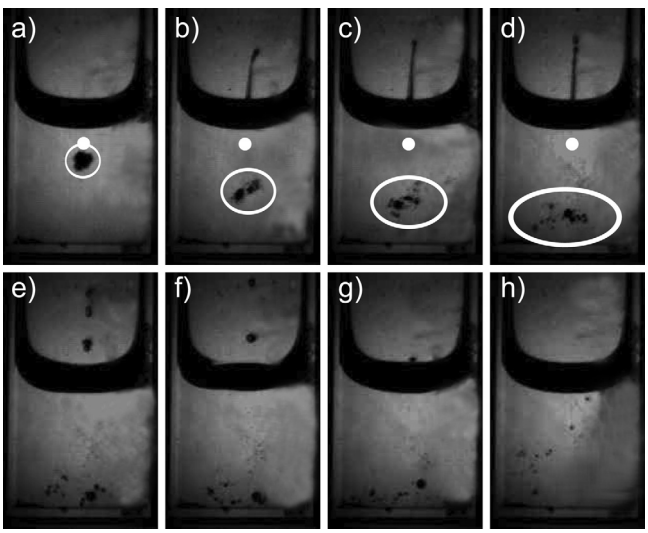

FIG. 2. Different stages in the dynamics of the saline solution after application of a laser pulse. (a) t = 0, (b) t = 2 ms, (c) t = 4 ms, (d) t = 8 ms, (e) 12 ms, (f) t = 18 ms, (g) t = 68 ms, and (h) t = 368 ms. In (a)-(d), the white dotted marks the position of the focal spot, and the white line surrounds the bubble cloud in each frame This is not provided in the lower row due to the fragmentation of the bubble cloud.

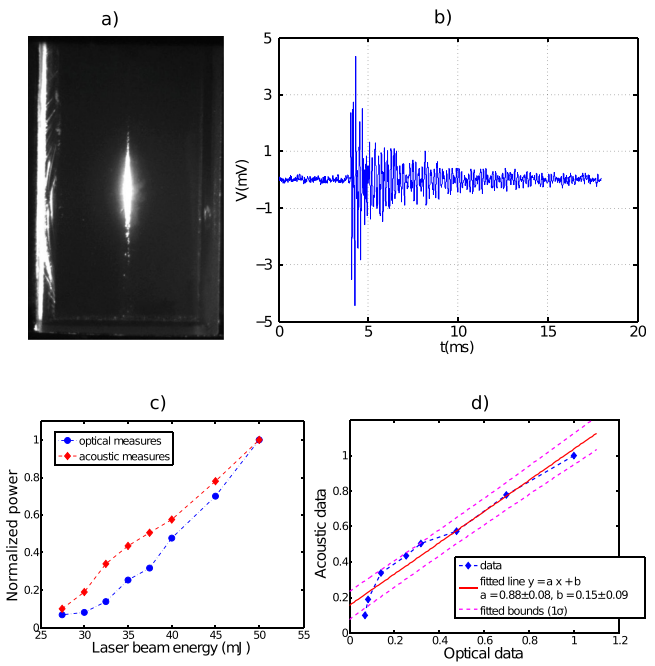

FIG. 3. (a) Image of the optical emission from the plasma generated by LIB in saline water as recorded with the slow CCD camera. (b) Oscilloscope trace of the acoustical signal as recorded by the microphone. (c) Optical (blue) and acoustic (red) intensity normalized to their maximum value as a function of pulse energy. (d) Correlation between the two variables.

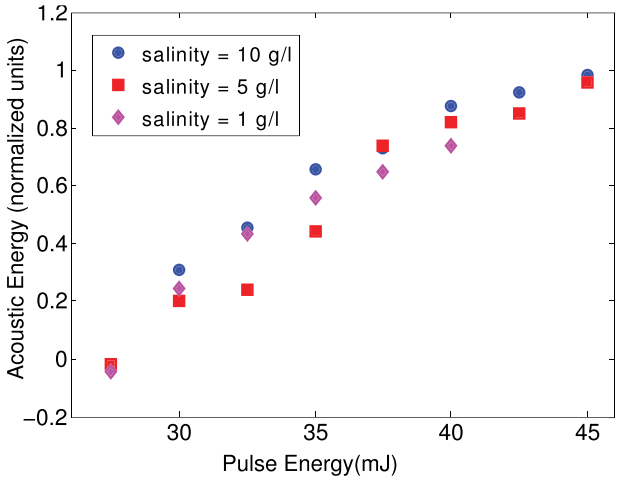

FIG. 4. Normalized acoustic energy for different pulse energies and salinities. Blue circles: 10 g/l, red squares: 5 g/l, and purple diamonds: 1 g/l.

a good linear correlation between them over the energy range explored. Therefore, any of them can be used to equally well to characterize the energy released in the process of LIB. This is very convenient because the acoustic signal can be processed in real time and the results stored by the digital scope in contrast with the analysis of the optical images that requires substantial and time-consuming post-processing. Hence, we shall henceforth use only the acoustic measurements for the characterization of the energy threshold for LIB of the saline solution.

Fig. 4 shows the normalized acoustic intensity as a function of pulse energy for different salinities of the solution. We observe a sublinear increase from zero for pulse energies above a threshold value which seems to be independent of salinity.

In order to quantitatively estimate the threshold energy, we fit the different data sets to the same functional form

$$P_{ac} = A_0[1 - e^{-\alpha(E-E_{th})}], \tag{1}$$

and we then average the three threshold values, which yields $E_{th} = 27.5 \pm 0.5$ mJ. Notice that this energy threshold is for the laser pulses at the laser output window. In principle, one could deduce the LIB intensity threshold from it if we knew the beam waist at the focal and the corrections due to the reflectivity at the air-quartz and quartz-water interfaces as well as the residual absorption of water. However, the large uncertainties in all these magnitudes result in a large spread of reported threshold values.[28] In our case, with an estimated beam waist $\simeq 20\,\mu$m, and assuming a residual reflectivity of 4% at the air-glass interfaces and a linear absorption of water of $0.4\,\text{cm}^{-1}$,[29] we obtain an irradiance threshold $I_{th} \simeq 350\,\text{GW/cm}^2$ which is about a factor 2 lower than the results reported by Docchio *et al.*[30] and Vogel[31] for distilled water and similar spot size, and only twice that reported by Toker *et al.*[32] for tap water and a bigger nominal spot size.

C. Pulse shielding

The bubble plume generated by a laser pulse around the focal spot is advected by the velocity field of the fluid.

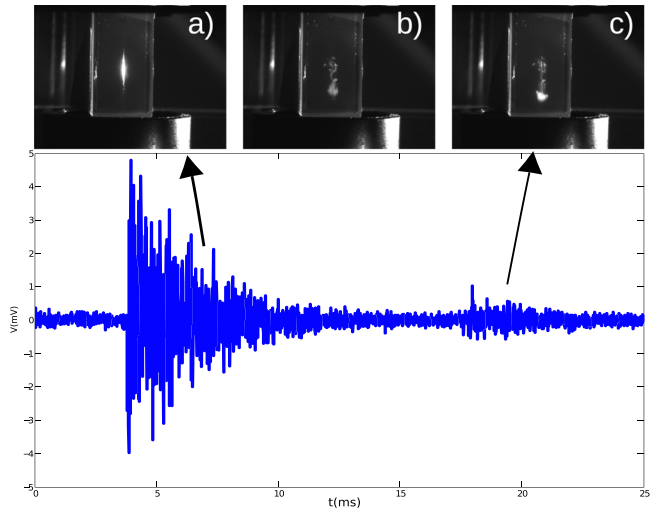

FIG. 5. Upper row: Typical CCD images of (a) the plasma emission induced by a first laser pulse launched from the bottom of the image, (b) the bubble cloud generated, and (c) scattered light and plasma emission induced by a second, almost completely blocked laser pulse. For these images, ethanol was added to the solution in order to better visualize the bubble cloud. Lower row: typical acoustic emission registered in this type of event. The arrows mark the portion of the acoustic wave associated with each pulse.

When a second laser pulse propagates through the plume, it is scattered by each bubble surface with a consequent decrease of the optical power in the vicinity of the focal spot and a reduction of the volume of fluid eventually vaporized in this region. This pulse shielding effect can be characterized by measuring the acoustic signal emitted by the second laser pulse (see Fig. 5). The knowledge of its dependence on the lapse between pulses is of obvious importance for applications. In Fig. 6, we show the ratio of the acoustic emission associated with each pulse, as a function of inter-pulse delay for different pulse energies and solution salinities.

All curves display essentially the same behaviour: a sudden increase of the ratio occurs for time delays of the order of $\sim$17 ms, and a plateau of high acoustic ratio is attained at delays longer than $\sim$22 ms. The value at this plateau is still

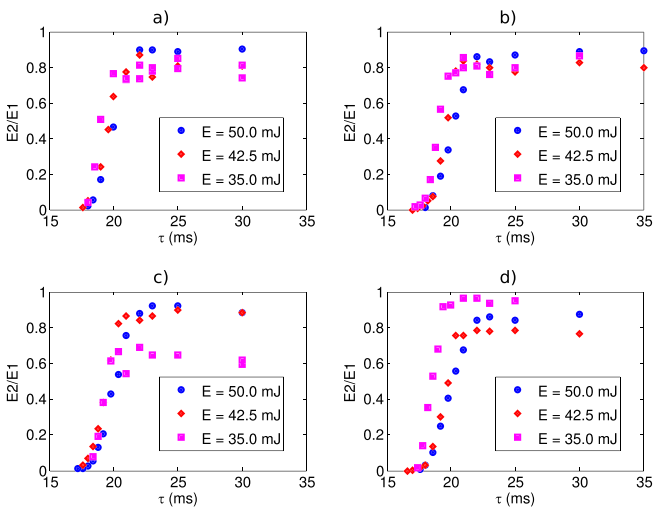

FIG. 6. Pulse shielding effect as a function of the delay between pulses for different salinities and pulse energies.

smaller than 1, a ratio that is only approached for delays of the order of 300 ms or longer, which implies that some degree of pulse shielding persists at inter-pulse time lapse scales of the order of 1 s.

The smooth transition reflects the statistical character of pulse shielding, which depends on the details of the evolution of the bubble plume. Because the bubble plume moves essentially downwards during the first stages of its evolution, the second pulse is almost totally blocked on. However, if the second pulse arrives when the bubbles start dispersing horizontally—sometimes because of the fluid motion but most often when they approach the bottom of the cuvette—it is blocked less efficiently by the bubble plume, with substantial fluctuations from one event to the other. For longer delays, most laser pulses pass with little scattering through the plume, giving rise to the plateau. However, the plateau does not reach 1 because of the few bubbles that remain in the optical path for long times until they melt or buoyancy drives them above the focal spot.

In order to characterize the dependence on the delay and for elucidating potential dependencies on pulse energy and salinity, we consider the different curves to have the same functional form

$$r = \frac{p}{2}\left[1 + \tanh\left(\frac{\tau - \tau_0}{\delta\tau}\right)\right]. \quad (2)$$

τ_0 corresponds to the delay time required for the attenuation by the bubble plume to reach 50% of the plateau value, p, and $\delta\tau$ describes how fast the transition from complete shielding to the plateau value occurs. These parameters are taken to depend on salinity and pulse energy, i.e.,

$$x = x_0 + x_1 s + x_2 E\,,\ x = \tau_0, \delta\tau\,. \quad (3)$$

A Bayesian fit is performed by assuming p to be purely random due to the fluctuations in the position of the microphone relative to the cuvette in the different measurements that require the replacement of the solution. The results of the fit are shown in Table I. We do not observe any significative dependence on salinity, but a linear dependence on pulse energy becomes apparent for both τ_0 and $\delta\tau$.

Since τ_0 basically corresponds to the time required for the bubble cloud to disperse in the horizontal direction, we attribute this slight increase with energy to the fact that more energetic pulses vaporize bigger fluid volumes; although the time required for the bubble plume to reach the bottom of the cuvette is almost independent on pulse energy, the larger the bubble plume the longer the time required for the bubble to disperse horizontally. Similarly, the increase of $\delta\tau$ with pulse energy can be attributed to the fact that, the higher the energy of the pulse, the larger the horizontal dispersion of the bubble before it reaches the bottom of the cuvette, hereby leading to a smoother transition from complete shielding to the plateau value.

TABLE I. Multi-linear parameter fit.

	x_0	x_1	x_2
p	0.84 ± 0.05	—	—
τ_0(ms)	16.1 ± 0.6	-0.02 ± 0.03	0.080 ± 0.014
$\delta\tau$(ms)	-0.75 ± 0.45	0.012 ± 0.018	0.04 ± 0.01

III. MODEL

In order to build a model to reproduce the experimental observations on pulse shielding, we need to consider three separate processes that occur on three different time scales: first, the propagation of light in a medium that presents nonlinear absorption and linear losses due to both scattering and absorption; second, the generation of the bubbles due to the laser pulse; and third, the movement of the bubbles in the fluid and how they interact with a second laser pulse.

We shall consider two laser pulses separated by some time delay travelling in a fluid that presents nonlinear, k-photon absorption. The first laser pulse will propagate in a homogeneous fluid at rest. The fluid will be completely vaporized at places where the density of energy absorption exceeds a prescribed threshold, yielding a cavitation bubble. The collapse of the cavitation bubble generates multiple bubbles concentrated in a small region of space. These bubbles move in the fluid due to advection and buoyancy. A second laser pulse will suffer additional losses due to scattering by the bubbles created by the first pulse, hereby reducing the size of the region where nonlinear absorption exceeds threshold. In the next subsections, we describe how these processes are included in the model.

A. Light distribution and energy deposition

We consider that the light field is composed of the laser beam and the scattered light, and only the former contributes to LIB in the vicinity of the focal spot. We consider that the propagation of the laser pulses can be described in the paraxial approximation as

$$\nabla_\perp^2 E + 2iq\left(\partial_z E + \frac{1}{v}\partial_t E\right) = -2iq\left(\alpha_k |E|^{2k} + \alpha_0\right)E, \quad (4)$$

where $q = \frac{2\pi n}{\lambda}$ is the optical wavevector and $v = (dq/d\omega)^{-1}$ is the group velocity. $\alpha_0(x, y, z, t)$ phenomenologically describes the losses due to both linear absorption in the fluid and scattering at each bubble surface, and $\alpha_k(x, y, z, t)$ describes the losses due to k-photon absorption in the medium. We have neglected group velocity dispersion because we are considering pulse durations of several ns, and we have also disregarded self-focusing because in our experimental conditions the propagation distances are much shorter than the characteristic length for self-focusing, which is ~ 1 m for an input power $P \sim 6$ MW.[33] In the reference frame $\xi = z$, $T = t - z/v$, Eq. (4) reads

$$\nabla_\perp^2 E + 2iq\partial_\xi E = -2iq(\alpha_k |E|^{2k} + \alpha_0)E. \quad (5)$$

Yet, no analytical solution of Eq. (5) is known, and sophisticated numerical tools are usually required in order to determine the beam profile upon propagation. However, an approximate solution can be found by means of the CVA extended to non conservative systems[24–26] like Eq. (5). The

left-hand side of Eq. (5) is the variational equation for E arising from the Lagrangian density

$$\mathcal{L} = iq(E^*\partial_\xi E - E\partial_\xi E^*) - |\nabla_\perp E|^2 . \quad (6)$$

The terms on the right-hand side of Eq. (5), R, are included by considering a trial function $E(x,y;p^{(1)}(\xi),\ldots,p^{(N)}(\xi))$ and constructing the reduced Lagrangian

$$L = \int\int \mathcal{L} dxdy, \quad (7)$$

which is a functional of $p^{(1)}(\xi),\ldots,p^{(N)}(\xi)$. The optimum choice is then determined by the system of equations

$$\frac{\partial L}{\partial p^{(j)}} - \frac{d}{d\xi}\frac{\partial L}{\partial p_\xi^{(j)}} = \int dx \int dy R \frac{\partial E}{\partial p^{(j)}}, \quad j = 1,2,\ldots N. \quad (8)$$

In order to apply the CVA to our problem, we assume axial symmetry of the beam because we are interested on the average pulse. Hence we take as trial function a beam of the form $E(x,y,z,t) = E(r,z,t) = A(\xi,T)\,\Phi(\xi,r)$, where $r^2 = x^2 + y^2$ and

$$\Phi(\xi,r) = \sqrt{\frac{2}{\pi}}\omega_0\mu(\xi)e^{-\mu(\xi)r^2}, \quad (9)$$

is a time-independent Gaussian beam of complex beam parameter

$$\mu(\xi) = \frac{1}{\omega_0^2}\frac{1}{1 + i(\xi - z_f)/z_R}, \quad (10)$$

such that ω_0 is the (minimum) beam waist and $z_R = q\omega_0^2/2$ is Rayleigh's length. The focal spot (the plane where the minimum waist is obtained in the absence of losses) is at z_f, and $\Phi(\xi, r)$ has been normalized such that $\int dx\,dy\,|\Phi|^2 = 1$ at any plane z.

For such a trial field, $A(\xi, T)$ describes the changes in the complex beam amplitude due to scattering and absorption and is our optimisation variable. Application of the CVA yields the evolution equation for the beam amplitude

$$\partial_\xi A = -(\bar{\alpha}_k|A|^{2k} + \bar{\alpha}_0)A, \quad (11)$$

where

$$\bar{\alpha}_l(\xi, T + \xi/v) = \frac{\int dxdy\alpha_l(x,y,\xi,T+\xi/v)|\Phi|^{2(l+1)}}{\int dxdy|\Phi|^2} . \quad (12)$$

These represent the transversally averaged losses—either linear ($l = 0$) or nonlinear ($l = k$)—that the laser beam experiences as it propagates, taking the transverse beam profile as the weight at each point. Defining

$$a_0(\xi,T) = \int_0^\xi \bar{\alpha}_0(x, T + x/v)dx \quad (13)$$

and

$$a_k(\xi,T) = 2k\int_0^\xi \bar{\alpha}_k(x, T + x/v)\, e^{-2ka_0(x,T)}dx, \quad (14)$$

one finally has that the longitudinal field profile in the CVA can be expressed as

$$A(\xi,T) = \frac{A_0(T)\, e^{-a_0(\xi,T)}}{\left[1 + a_k(\xi,T)|A_0(T)|^{2k}\right]^{1/(2k)}} . \quad (15)$$

In many cases of interest, the medium occupies a finite region $0 < z < h$; in addition, often the multiphoton absorption coefficient does not depend on either time or space when within the medium—i.e., $\alpha_k(\vec{r},t) = \alpha_k\,[\Theta(z) - \Theta(z-h)]$, where $\Theta(z)$ is Heaviside's step function. With these assumptions, it is found that

$$\bar{\alpha}_k(\xi,T) = \frac{\alpha_k}{k+1}\left(\frac{2}{\pi}\right)^k \frac{\Theta(\xi) - \Theta(\xi - h)}{\omega(\xi)^{2k}}, \quad (16)$$

independent of time, with $\omega(\xi) = \omega_0\left[1 + \left(\frac{\xi - z_f}{z_R}\right)^2\right]^{1/2}$ being the beam waist at the different propagation planes. Since the beam diameter is minimum at the focal point, Eq. (16) reflects that the effective nonlinear loss of the beam is maximal in the vicinity of the focal plane, where the beam waist is at its minimum.

Therefore, in terms of the original variables, the laser field in the CVA is distributed at any time according to

$$E(x,y,z,t) = A(z,t)\,\Phi(x,y,z),$$
$$A(z,t) = \frac{A_0(t - z/v)\, e^{-a_0(z,t-z/v)}}{\left[1 + a_k(z,t - z/v)|A_0(t - z/v)|^{2k}\right]^{1/(2k)}}, \quad (17)$$

and computing it at the entry plane $z = 0$ determines that $|A_0(t)|^2 \sim P(t)$, the power emitted by the laser that penetrates in the medium at time t. It is worth remarking that the decay of field profile clearly departs from the usual Lambert's law due to the polynomial term in the denominator. In a transparent medium, $a_0 \equiv 0$, and all the dissipation occurs in the vicinity of the focal spot, where the effective nonlinear loss is the highest.

Once $\alpha_0(\vec{r},t)$ is known, the CVA approximation for the field distribution in the medium is completely prescribed. As already commented, $\alpha_0(\vec{r},t)$ phenomenologically describes both linear absorption in the medium and light scattering at each bubble surface. The former contribution is quite small in our experiment and will be neglected henceforth, while the second will be discussed in detail below.

B. Bubble formation and transport

The bubble cloud results from the collapse of the cavitation bubble induced by LIB, which we consider that happens—as in the blow-off model[34,35]—in the region where the flux density exceeds the threshold value. This corresponds to an energy density absorbed from the laser pulse by multiphoton processes, $U_{mp}(\vec{r},t)$, above a threshold, $\mathcal{E}_{th}$.

At a fixed location, the power density absorbed by multi-photon processes is given by

$$\partial_t U_{mp} = 2\varepsilon_0 n^2 v\alpha_k|E|^{2(k+1)}, \quad (18)$$

and it can be readily computed in the CVA by direct integration of the field profile.

The total energy conveyed to the breakdown process by the laser beam at time t is

$$\mathcal{E}_{abl}(t) = \int (U_{mp}(\vec{r},t) - \mathcal{E}_{th})\Theta(U_{mp}(\vec{r},t) - \mathcal{E}_{th})\, d^3r, \quad (19)$$

where the region of integration is the space occupied by the fluid, although the step function restricts it to the breakdown region where the energy density exceeds the threshold. Since the formation of the bubble cloud occurs on long time scales as compared to the duration of the pulse, one can take $\mathcal{E}_{abl} = \mathcal{E}_{abl}(t \to \infty)$ as the energy available for generation of the bubbles, and also as a measure of the acoustic emission, i.e., we take $P_{ac} = \mathcal{E}_{abl}$. Similarly, the total energy absorbed by the fluid in a multi-photon processes is given by

$$\mathcal{U}_{mp} = \int U_{mp}(\vec{r}, t \to \infty)\, d^3r, \quad (20)$$

where now the region of integration extends to the whole fluid.

To model the process of formation of the bubble cloud, we recall that creating a bubble has an energy cost that depends on the bubble radius, the vapor-fluid surface tension and the pressure excess of the bubble. Since the collapse of the cavitation bubble that generates the bubble cloud is stochastic and originates multiple bubbles of different sizes, we consider that the radius of each bubble—hence its energetic cost—is randomly distributed according to a log-normal distribution.[36] The amount of energy initially available for bubble formation is $\mathcal{E}^0_{abl} = \mathcal{E}_{abl}$ and we proceed sequentially to generate bubbles. At each step, the energy available for bubble formation is $\mathcal{E}^n_{abl}$, and we pick one energy cost, $\mathcal{E}_{bub}$, from the log-normal distribution. If this energy cost is smaller than $\mathcal{E}^n_{abl}$, we update the energy available for bubble formation to $\mathcal{E}^{n+1}_{abl} = \mathcal{E}^n_{abl} - \mathcal{E}_{bub}$ and we repeat the process again; otherwise, the random pick of energy is repeated. If no suitable bubble energy can be obtained after ten trials, we conclude that the energy available for bubble formation at this fluid parcel is too low and stop the iteration process. Finally, the N_b bubbles generated are uniformly distributed across the ablation region.

For the bubble movement, we consider a simple, Lagrangian dynamics where the velocity of each bubble relative to the fluid is limited by Stokes force. In this approximation, the dynamics of each bubble is described by

$$d_t\vec{r}_i = \vec{V}(\vec{r}_i, t) + \vec{v}_i,$$
$$d_t\vec{v}_i = \vec{g} - f\,[\vec{v}_i - \vec{V}(\vec{r}_i, t)] + \vec{\xi}_i,$$

where $\vec{r}_i$ is the position of the bubble, $\vec{v}_i$ is its velocity relative to the fluid—whose velocity field $\vec{V}(\vec{r},t)$, will be discussed in next subsection—, $\vec{g}$ is the buoyancy force, f is the Stoke's parameter and $\vec{\xi}_i$ is a stochastic term intended to simulate both fluid turbulence and diffusion effects.

Finally, the attenuation of the laser beam due to scattering by the bubble distribution is given by

$$\alpha_0(\vec{r},t) = \sum_{i=1}^{N_b} \alpha_i \delta(\vec{r} - \vec{r}_i(t)), \quad (21)$$

where α_i is the scattering coefficient of bubble i. For the sake of simplicity, we take the same value for all bubbles, $\alpha_i = \alpha_F$.

C. Fluid motion: Pressure and velocity fields

Nonlinear absorption of the laser pulses represents a localized heat deposition that generates a pressure and velocity field in the fluid. The linearized pressure field is described by[37]

$$\partial_t^2 p - c_s^2 \nabla^2 p = (\gamma - 1)\partial_t H, \quad (22)$$

where c_s is the (linear) speed of sound, γ is the adiabatic coefficient of the fluid and H is the deposition rate of heat in the fluid. Defining the potential $\Psi(\vec{r},t)$ such that $p = -\partial_t\Psi$, then the velocity field can be found as $\vec{V} = \vec{\nabla}\Psi$, and the potential equation reads

$$\nabla^2\Psi - \frac{1}{c_s^2}\partial_t^2\Psi = -\frac{\gamma - 1}{c^2}H. \quad (23)$$

We consider that, on hydrodynamical scales (i.e., space scales of 0.1 mm or larger and time scales of the order of 1 ms or longer), H can be taken as completely localized, so that $H = h(t)\delta(\vec{r} - \vec{r}_f)$, with $\vec{r}_f = (0,0,z_f)$ being the position of the focal spot. On hydrodynamical time scales much longer than the pulse duration, one can take

$$h(t) = \mathcal{U}_{mp}\frac{e^{-\lambda t}}{\lambda}\Theta(t), \quad (24)$$

where $\mathcal{U}_{mp}$ is the total energy absorbed in the fluid by multiphoton processes, and λ is a decay constant intended to phenomenologically account for, e.g., the decay due to thermal conduction. Thus, we finally have that

$$\nabla^2\Psi - \frac{1}{c_s^2}\partial_t^2\Psi = a(t)\delta(\vec{r} - \vec{r}_f), \quad (25)$$

where $a(t) = -(\gamma - 1)h(t)/c^2$. Yet, determining the potential is a formidable problem in computational fluid dynamics, especially when moving boundaries and multiple fluid phases come into play. We shall hence adopt a phenomenological approach intended to reproduce the main features of the shielding phenomenon described in the previous section. Initially, the fluid-air interface is at $z = h$, and the fluid occupies the region $0 < z < h$. At the fluid-air interface, the fluid velocity must be purely normal to the interface, while at the rigid bottom ($z = 0$), the fluid velocity must be tangential to the boundary. Disregarding the effects of the sidewalls and the deformation of the fluid-air interface, the solution to Eq. (25) can be determined by the method of images[38] as an infinite series,

$$\Psi(\vec{r},t) = \frac{1}{4\pi}\sum_k \frac{a_k(t - \tau_k)}{|\vec{r} - \vec{r}_k|}, \quad (26)$$

where $a_k(t)$ are the effective source strengths, located at $\vec{r}_k = (0,0,z_k)$, and $\tau_k = \frac{|\vec{r} - \vec{r}_k|}{c_s}$ is the propagation delay from source k to point $\vec{r}$. The source strengths $a_k(t)$ and positions $\vec{r}_k$ are chosen in order to satisfy the boundary conditions for the problem. In our case, the first four terms of the series

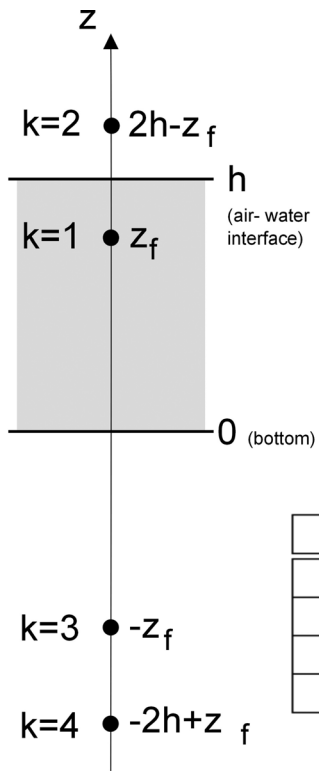

k	$a_k(t)$
1	$a(t)$
2	$-a(t)$
3	$a(t)$
4	$-a(t)$

FIG. 7. Sketch of the source distribution used to compute the fluid flow, with their positions and values. The grey area corresponds to the region occupied by the fluid.

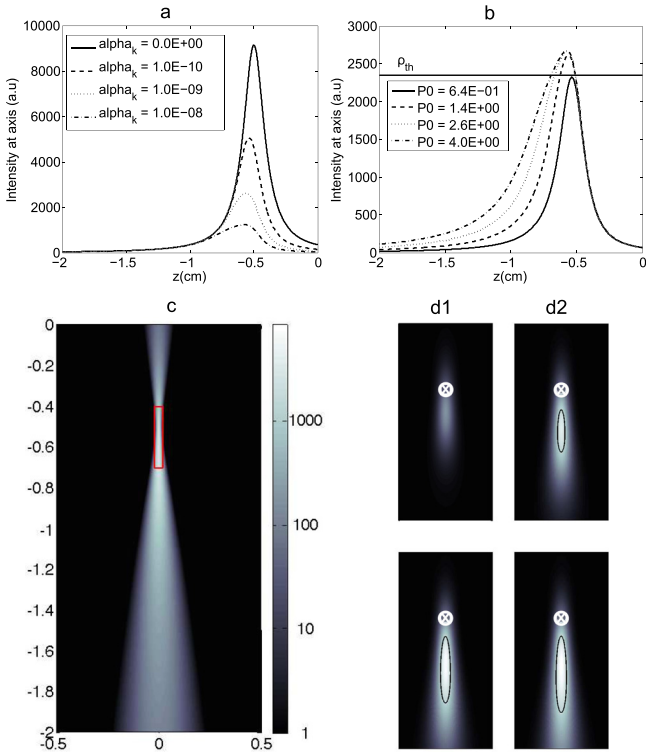

FIG. 8. Beam profiles. (a) Beam profile obtained for different values of the nonlinear absorption coefficient (in cm^{-1}) for a fixed input power $P_0 = 1.4$. (b) Beam profile for different values of the input power, for a fixed nonlinear absorption coefficient $\alpha_K = 10^{-9}\,\mathrm{cm}^{-1}$. (c) Two-dimensional plot of the EM energy in the dominium, represented in a color-gradient logscale. The region inside the red box is zoomed-in in subfigures d1-d4, where we plot $\mathcal{U}_{mp}(\vec{r}, t \to \infty)$ for the different input powers used in (b). In each subfigure, the position of the beam waist in the transparent case is denoted by $\otimes$, while the black contour indicates the region where the density of nonlinearly absorbed energy exceeds the ablation threshold. d1 shows no contour, because the threshold is not reached, and no LIB phenomenon occurs. In d2-4 the LIB contour occurs before the beam reaches the focal point.

already provide a rather satisfactory approximation to the flow, with the source and position values given in Fig. 7.

D. Results

In this section, the theoretical results are presented for four-photon absorption processes ($K = 3$). The beam parameters are taken from the experiment, and the electric field is normalized to the breakdown value obtained experimentally ($|E| \sim 10^7$ V/m, which corresponds to a breakdown intensity $I \sim 400\,\mathrm{GW/cm}^2$). The beam power is thus normalized to the threshold value, and the normalized four-photon absorption coefficient is taken as $\alpha_3 = 10^{-9}\,\mathrm{cm}^{-1}$. The scattering coefficient for the bubbles is $\alpha_F = 6\ 10^{-5}\,\mathrm{cm}^{-1}$, the speed of sound $c_s = 10^5$ cm/s, gravity $g = 10^3\,\mathrm{cm/s}^2$ and Stokes friction coefficient is $f = 10^3\,\mathrm{s}^{-1}$. As already commented, for the sake of simplicity, we neglect linear absorption in water, which is $\alpha_0 = 0.13\,\mathrm{cm}^{-1}$ at 1064 nm.

The first laser pulse propagates in a homogeneous medium where no bubbles are formed, hence it experiences multiphoton absorption only. The CVA beam profile obtained in this case is depicted in the Fig. 8(a) for different values of α_k for a laser beam coming from the bottom. One can see that the most prominent effect of nonlinear absorption is to distort the beam profile, leading to an advancement of the point of maximum intensity with respect to the waist plane of the beam. Accordingly, the point of maximum nonlinear absorption moves towards the light source. The larger the nonlinear absorption coefficient, the bigger this displacement.

A similar effect also occurs for fixed nonlinear absorption coefficient α_k when the beam power is increased (see Fig. 8(b)). For low pulse power ($P_0 = 0.64$), nonlinear absorption has no noticeable effects, and the beam propagates with very small loses and keeping a symmetric distribution with respect to the waist plane, located at $z = -0.5$. As the input power grows, the position where the beam reaches its peak power moves progressively towards the source and the peak power tends to saturate and to develop a plateau at very high input powers. After the focal plane, the beam profile is almost independent of the input power, reflecting that the higher the input power, the higher the energy lost before the focal is reached, and almost all the beam energy is absorbed in a very small spatial interval before the focal spot.

If the input power is too low, the threshold for LIB is not reached anywhere in the fluid (Fig. 8, d1). As the input power increases, the region where the absorbed energy exceeds the threshold progressively grows (see the black contour line in Fig. 8, d2–d4).

The ablation energy $\mathcal{E}_{abl}$ as function of beam power can then be computed using Eq. (19), and it is plot in Fig. 9. It is seen that $\mathcal{E}_{abl}$ grows sublinearly with input power, in good agreement with the acoustic measurements shown in Fig. 4. This sublinearity stems from the non-exponential decay of the field amplitude in Eq. (17) that implies a saturation of the

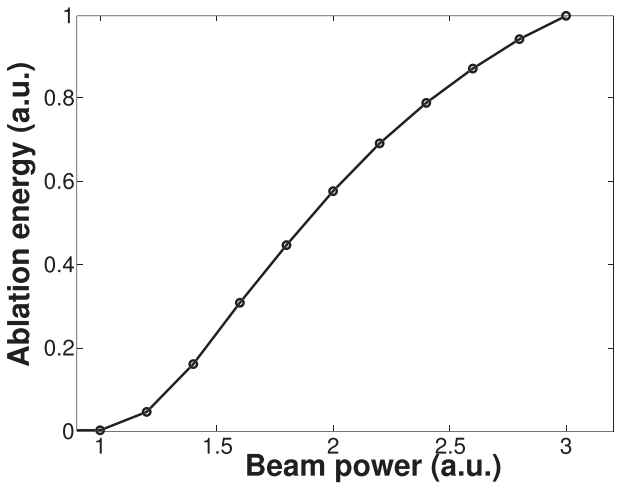

FIG. 9. Ablation energy of one pulse.

maximum density of electromagnetic energy in the medium as the input power grows. This saturation effect overcompensates the increase of the volume of fluid where the threshold is surpassed, leading to a sublinear growth of the ablation energy.

When LIB occurs, bubbles form in the breakdown region and subsequently evolve driven by the velocity field induced in the fluid. Thus, the spatial distribution of the bubbles varies in time, as shown in Fig. 10. The bubble cloud moves mostly downwards, with an average speed that increases with pulse energy. Notice, however, that a slight spread of the plume is evident even on short times. The spread of the bubble cloud can be explained by the structure of the fluid flow. On short time scales, it is dominated by the point-wise character of the pressure source, together with the fact that the ablation region is located before this point. On longer time scales, as the plume evolves towards the bottom of the cell, boundary effects dominate and stronger horizontal components appear in the velocity due to the impenetrability of the wall.

If a second laser pulse were sent while the bubble cloud is present, the beam would experience scattering by the bubbles and part of its power would not reach the focus region. As a consequence ablation energy in the fluid would decrease. The shielding effect can be characterized by the ratio $\mathcal{E}_{abl,2}/\mathcal{E}_{abl,1}$, where $\mathcal{E}_{abl,j}$ denotes the ablation energy of pulse j as given in Eq. (19). Figure 11 shows this ratio as function of the delay time between the pulses, where the labeled points correspond to the times selected for plotting the bubble distribution in Fig. 10. The ratio has the shape of a rather sharp sigmoid varying from 0 at short times (complete blocking) to 1 at long times (no blocking). This shape reflects the different state of the environment traversed by the second pulse as the delay increases. If the delay is short, like in points a and b, the bubble cloud still lies close to the focal spot and is concentrated around the optical axis, hence the second pulse will experience strong scattering by the bubbles that will prevent reaching the LIB threshold and complete shielding of the second pulse will occur. As soon as the bubble cloud starts to spread horizontally (point c), the scattering reduces and the LIB threshold is surpassed in a small volume of the fluid. For long delays (point d and later), the bubble cloud has completely spread out of the optical path. The beam is then not blocked and the ratio approaches 1.

The model provides a good qualitative explanation for the shielding process observed experimentally. Notice, however, that plateau in the experimental results corresponds to $\mathcal{E}_{abl,2}/\mathcal{E}_{abl,1} < 1$. This discrepancy originates from the fact that in our model, we are not considering the boundary effects due to the finite lateral size of the cell. The lateral walls limit the horizontal motion of the fluid, keeping the

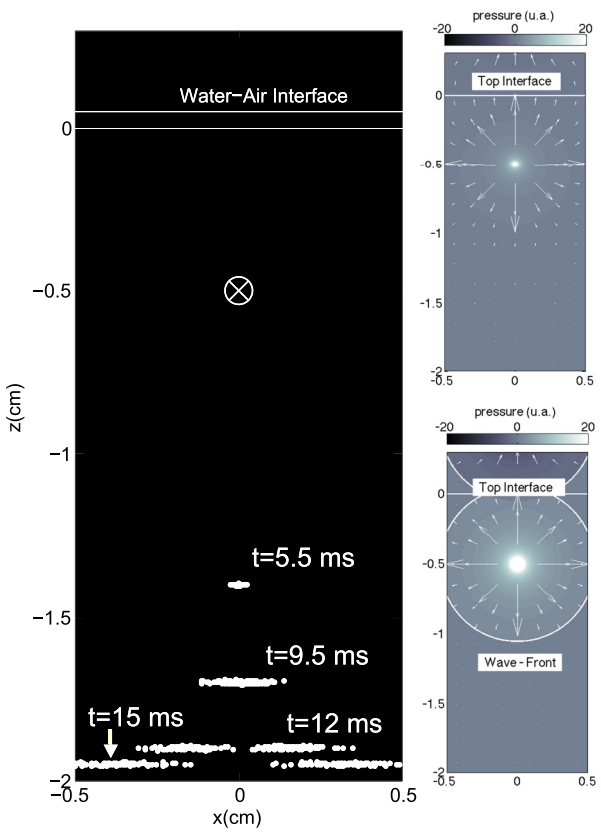

FIG. 10. Left column: Bubble distribution at different times (indicated in the figure) after a pulse of power $P = 3$ is sent into the fluid. The focal spot is marked with ⊗. Right column: sketches of the pressure (up) and velocity field (bottom) induced by the pulse.

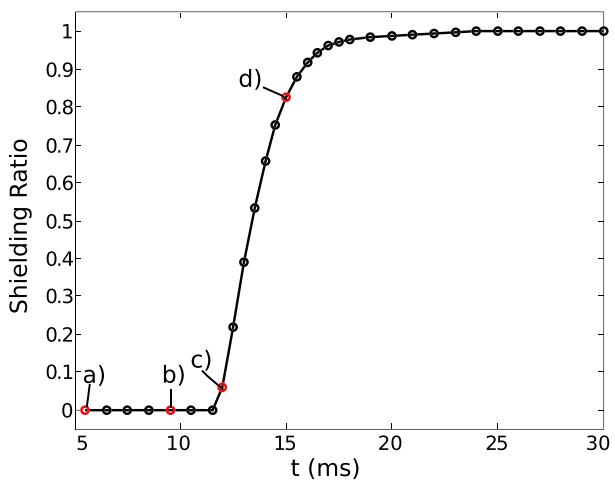

FIG. 11. Shielding coefficient as a function of the delay between pulses for the same conditions as in Fig. 10. The points marked in color correspond to the times used to plot the bubble cloud in Fig. 10.

bubbles near the optical axis for longer timer than those considered in the model. These effects give rise to a long-lived distribution of bubbles that will produce a residual attenuation of the beam until times long enough for buoyancy to take over and remove them from the optical path.

IV. CONCLUSIONS

We have studied experimentally and theoretically the pulse shielding in Laser-Induced Breakdown of saline water on hydrodynamic time scales. We have characterized the acoustic energy released by pulses from a Nd:YAG laser focused into a saline solution. Pairs of pulses were delivered with a controlled time delay between them. The first pulse allows to extract the threshold intensity for LIB. The shielding effect on the second pulse has been characterized as a function of salinity, pulse energy, and interpulse time. A phenomenological model for the shielding process of the second pulse has been developed making use of the Collective Variable Approach. The model includes nonlinear absorption and scattering by the bubble cloud, and the evolution of the latter under the action of buoyancy and advection. A significant departure from exponential decay is obtained for the beam profile due to nonlinear absorption. The model allows us to explain satisfactorily the observed dependencies on pulse energy and delay.

ACKNOWLEDGMENTS

We acknowledge technical support from Dr. Luca Furfaro (U. du Franche-Compté), and funding from the Direcció General de Recerca, Desenvolupament Tecnològic i Innovació de la Conselleria d'Innovació, Interior i Justícia del Govern de les Illes Balears co-funded by the European Union FEDER funds. J.J. acknowledges financial support from the Ramon y Cajal fellowship. F. Marino acknowledges partial financial support from UIB.

[1]D. Bauerle, *Laser Processing and Chemistry* (Springer, Berlin/Heidelberg, 2011).
[2]M. H. Niemz, *Laser-Tissue Interactions: Fundamentals and Applications*, Biological and Medical Physics, Biomedical Engineering (Springer, Berlin/Heidelberg, 2004).
[3]F. Hillenkamp and M. Karas, Int. J. Mass Spec. **200**, 71 (2000).
[4]D. Chrisey and G. Hubler, *Pulsed Laser Deposition of Thin Films* (Wiley-Interscience, 1994).
[5]J. Jersch, F. Demming, J. Hildenhagen, and K. Dickmann, Opt. Laser Technol. **29**, 433 (1998).
[6]A. Puretzky, D. Geohegan, X. Fan, and S. Pennycook, Appl. Phys. A **70**, 153 (2000).
[7]Y. F. Zhang, Y. H. Tang, N. Wang, D. P. Yu, C. S. Lee, I. Bello, and S. T. Lee, App. Phys. Lett. **72**, 1835 (1998).
[8]J. Fitz-Gerald, S. Pennycook, H. Gao, and R. Singh, Nanostructured Mater. **12**, 1167 (1999).
[9]P. Ayyub, R. Chandra, P. Taneja, A. Sharma, and R. Pinto, Appl. Phys. A **73**, 67 (2001).
[10]W. Lauterborn and A. Vogel, in *Bubble Dynamics and Shock Waves*, Shock Wave Science and Technology Reference Library Vol. 8, edited by C. F. Delale (Springer, Berlin/Heidelberg, 2013), pp. 67–103.
[11]A. Vogel and V. Venugopalan, Chem. Rev. **103**, 577 (2003).
[12]Note1, in cases where material débris are also present—and subject also to advection by the fluid flow—both bubbles and débris will contribute additively to the scattering and absorption of the laser light.
[13]K. Nahen and A. Vogel, J. Biomed. Opt. **7**, 165 (2002).
[14]A. K. Murray and M. R. Dickinson, Phys. Med. Biol. **49**, 3325 (2004).
[15]K. Sasaki, T. Nakano, W. Soliman, and N. Takada, Appl. Phys. Express **2**, 046501 (2009).
[16]A. Vertes, P. Juhasz, M. D. Wolf, and R. Gijbels, Int. J. Mass Spectrosc. Ion Processes **94**, 63 (1989).
[17]G. Callies, H. Schittenhelm, P. Berger, and H. Hügel, Appl. Surf. Sci. **127–129**, 134 (1998).
[18]I. Zinovik and A. Povitsky, J. Appl. Phys. **100**, 024911 (2006).
[19]K. Pathak and A. Povitsky, J. Appl. Phys. **104**, 113108 (2008).
[20]G. Dumitru, V. Romano, and H. Weber, Appl. Phys. A **79**, 1225 (2004).
[21]F. Brandi, N. Burdet, R. Carzino, and A. Diaspro, Opt. Express **18**, 23488 (2010).
[22]P. Mulser and D. Bauer, *High Power Laser-Matter Interaction*, Springer Tracts in Modern Physics, Vol. 238 (Springer, 2010).
[23]D. Anderson, Phys. Rev. A **27**, 3135 (1983).
[24]D. Anderson, M. Lisak, and A. Berntson, Pramana **57**, 917 (2001).
[25]J. Hermann, Opt. Commun. **217**, 421 (2003).
[26]D. Ianetz, Y. Kaganovskii, and A. Wilson-Gordon, Opt. Commun. **285**, 3636 (2012).
[27]D. Kim, M. Ye, and C. Grigoropoulos, Appl. Phys. A **67**, 169 (1998).
[28]A. D. Giacomo, M. Dell'Aglio, O. D. Pascale, and M. Capitelli, Spectrochim. Acta Part B: Atom. Spectrosc. **62**, 721 (2007).
[29]G. M. Hale and M. R. Querry, Appl. Opt. **12**, 555 (1973).
[30]F. Docchio, A. Avigo, and R. Palumbo, EPL (Europhysics Letters) **15**, 69 (1991).
[31]A. Vogel, K. Nahen, D. Theisen, and J. Noack, IEEE J. Select. Top. Quantum Electron. **2**, 847 (1996).
[32]G. Toker, V. Bulatov, T. Kovalchuk, and I. Schechter, Chem. Phys. Lett. **471**, 244 (2009).
[33]R. Menzel, *Photonics: Linear and Nonlinear Interactions of Laser Light and Matter*, 2nd ed. (Springer, Berlin/Heidelberg, 2007).
[34]R. Srinivasan and V. Mayne-Banton, Appl. Phys. Lett. **41**, 576 (1982).
[35]J. E. Andrew, P. E. Dyer, D. Forster, and P. H. Key, Appl. Phys. Lett. **43**, 717 (1983).
[36]P. Lage and R. Espósito, Powder Technol. **101**, 142 (1999.
[37]A. Miklos, P. Hess, and Z. Bozoki, Rev. Sci. Instrum. **72**, 1937 (2001).
[38]J. B. Allen and D. A. Berkley, J. Acoust. Soc. Am. **65**, 943 (1979).